



Well-designed β - Ag_2MoO_4 crystals with photocatalytic and antibacterial activity



Cibele A. Oliveira^a, Diogo P. Volanti^{b,*}, André E. Nogueira^c, Camila A. Zamperini^d, Carlos E. Vergani^a, Elson Longo^a

^a Center for the Development of Functional Materials, UNESP - Univ Estadual Paulista, Avenida Professor Francisco Degni, 55, Araraquara 14800-900, Brazil

^b Laboratory of Materials for Sustainability, IBILCE, UNESP - Univ Estadual Paulista, Rua Cristóvão Colombo, 2265, S. J. Rio Preto 15054-000, Brazil

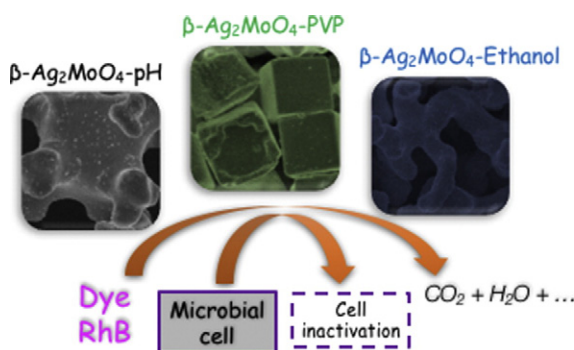
^c Embrapa Instrumentation, Rua XV de Novembro, 1452, São Carlos 13560-970, Brazil

^d University of Illinois at Chicago, South Paulina Street, 801, Chicago 60612-7212, USA

HIGHLIGHTS

- β - Ag_2MoO_4 with controlled morphologies were prepared by the microwave-assisted solvothermal method.
- β - Ag_2MoO_4 obtained under controlled pH exhibited the best Rhodamine-B photodegradation.
- β - Ag_2MoO_4 synthesized in ethanol medium highlight the potential application for *E. coli* bacteria control.
- The β - Ag_2MoO_4 properties can be attributed to the splitting of the electron-hole pairs in its complex cluster.

GRAPHICAL ABSTRACT



ARTICLE INFO

Article history:

Received 9 September 2016

Received in revised form 6 November 2016

Accepted 8 November 2016

Available online 11 November 2016

Keywords:

Silver molybdate

Photodegradation

Antibacterial

Multifunctional

Crystal growth

ABSTRACT

This paper describes the beta silver molybdate (β - Ag_2MoO_4) samples with spinel-type cubic structures synthesized with various morphologies, including round tips coral-like, elongated coral-like and truncated cube, by the microwave-assisted solvo-/hydrothermal method. The crystal morphologies could be controlled by adjusting the solvent, surfactant, and pH of the precursor solution. X-ray diffraction, field-emission scanning electron microscopy, Fourier-transform Raman spectroscopy, and diffuse reflectance spectroscopy in the ultraviolet-visible (UV-Vis) region, were used to characterize the structures of the samples. The specific surface area was determined using the Brunauer–Emmett–Teller method. Furthermore, the photocatalytic/antibacterial properties of the particles were dependent on the β - Ag_2MoO_4 crystal morphology and were evaluated by Rhodamine B dye photodegradation under UV-Vis light, and by determining their minimum inhibitory and bactericidal concentrations, using a broth microdilution assay for *Escherichia coli* bacteria.

© 2016 Elsevier Ltd. All rights reserved.

1. Introduction

The control of size and morphology of molybdate compounds plays a fundamental role in the improvement for organic pollutant degradation

in wastewater [1–4], and to antibacterial applications [5–7]. For this purposes, traditionally, several synthesis methods, including co-precipitation [8], hydrothermal [9], solvothermal [10], sonochemical [11], and sol-gel [12], have been used to produce these materials. By varying the synthesis parameters, such as the pH, temperature, and precursors, these materials can exhibit different morphologies [8,13]. Like this, Singh et al. [13], studied the influence of pH on flower-like $\text{Ag}_2\text{Mo}_2\text{O}_7$

* Corresponding author.

E-mail address: volanti@ibilce.unesp.br (D.P. Volanti).

assembled. Nagaraju et al. [14], synthesized wire-like, nanorod, and multi-pod forms of the $\text{Ag}_6\text{Mo}_{10}\text{O}_3$ and $\text{Ag}_2\text{Mo}_2\text{O}_7$. Qian et al. [15], obtained a cube-like $\text{Ag-Ag}_2\text{MoO}_4$ composite. Also, Ng et al. [16], synthesized $\alpha\text{-Ag}_2\text{MoO}_4$ spherical microcrystals under ambient conditions using 3-bis(2-pyridyl)pyrazine doping. Thus, all these earlier studies have been proposed to improve the molybdates properties for a specific application either by varying the methods or by some synthesis parameters.

Among molybdate compounds, the beta silver molybdate ($\beta\text{-Ag}_2\text{MoO}_4$) with cubic spinel structure [16], and the energy gap of 3.26–3.41 eV have received extensive attention as possible solutions for semiconductor technology [17,18]. However, few studies have been focused on the fine-tuning accelerated microwave-assisted solvo-/hydrothermal synthesis which improves the synthesis time of the $\beta\text{-Ag}_2\text{MoO}_4$ material. Therefore, the main motivation of this research was to obtain controlled $\beta\text{-Ag}_2\text{MoO}_4$ morphologies with an active and specific surface for improving their photocatalytic/antibacterial performance. Furthermore, to the best of our knowledge, none previous research has used $\beta\text{-Ag}_2\text{MoO}_4$ particles for the destruction of *E. coli* bacteria.

An efficient photocatalyst should have a wide-ranging photoabsorption and the electrons and holes photogenerated during the photocatalysis process should have a low recombination rate. However, prompt recombination of the photoinduced electron-hole pairs limits the photocatalytic efficiency of the material [19]. On the other hand, while the mechanism of bacterial activity has been significant advances, it is still not fully understood. Earlier studies indicated that the reactive oxygen species and hydrogen ions cause protein inactivation and consequent bacteria apoptosis [20–22]. Hence, it is necessary to understand the photodegradation/decontamination mechanisms of the $\beta\text{-Ag}_2\text{MoO}_4$ -based materials to become the process more efficient.

This paper describes the microwave-assisted solvo-/hydrothermal synthesis and crystal growth mechanism of three new kinds of well-designed $\beta\text{-Ag}_2\text{MoO}_4$ morphologies (round tips coral-like, elongated coral-like and truncated cube) with photocatalytic and antibacterial activity. Also, the antibacterial activity of these particles was evaluated by determining their minimum inhibitory and bactericidal concentrations (MIC and MBC), using a broth microdilution. This study provides the development of the photocatalytic, and antibacterial mechanism of the $\beta\text{-Ag}_2\text{MoO}_4$ crystals which can be attributed to the splitting of the electron-hole pairs in its cluster-like structure ($[\text{MoO}_4]_o/[\text{MoO}_4]_d$ or $[\text{AgO}_6]_o/[\text{AgO}_6]_d$).

2. Materials and methods

2.1. Materials

Sodium molybdate dihydrate ($\text{Na}_2\text{MoO}_4 \cdot 2\text{H}_2\text{O}$, 99.5% purity), molybdic acid (H_2MoO_4 , 85% purity), silver nitrate (AgNO_3 , 99% purity), absolute ethanol ($\text{C}_2\text{H}_6\text{O}$, Synth), and potassium hydroxide (KOH, 3 M) were obtained from Sigma-Aldrich.

2.2. Poly(vinylpyrrolidone) (PVP)-assisted synthesis

Aggregates of $\beta\text{-Ag}_2\text{MoO}_4$ particles were synthesized by separately dissolving 2 mmol of AgNO_3 and 1 mmol of $\text{Na}_2\text{MoO}_4 \cdot 2\text{H}_2\text{O}$ in two tubes, respectively, which contained deionized water (50 mL) [18]. Subsequently, 1 g of poly(vinylpyrrolidone) (PVP) was placed into the tube that contained $\text{Na}_2\text{MoO}_4 \cdot 2\text{H}_2\text{O}$, and the mixture was subjected to ultrasonication for 15 min. The two solutions were then transferred to a Teflon autoclave with a capacity of 100 mL, which was subsequently sealed. The autoclave was placed into a microwave-assisted solvo-/hydrothermal system (2.45 GHz, maximum power of 850 W) [23], which was held at 150 °C for 1 h and subsequently cooled to room temperature. The resulting solution was washed four times and centrifuged twice with water and twice with absolute ethanol, over a period of

10 min, and only these samples were also washed with acetone. The resultant solution had a pH of 7.0. A violet-colored precipitate was obtained, which was dried in an oven for 12 h. Three samples were prepared and analyzed to evaluate the reproducibility of the method. The samples prepared by this procedure were denoted as $\beta\text{-Ag}_2\text{MoO}_4\text{-PVP}$.

2.3. Ethanol-assisted synthesis

A similar procedure to that used above was used to prepare samples that were denoted as $\beta\text{-Ag}_2\text{MoO}_4\text{-Ethanol}$; however, during this procedure, the PVP was not added. To synthesize the Ag_2MoO_4 particles, 2 mmol of AgNO_3 and 1 mmol of $\text{Na}_2\text{MoO}_4 \cdot 2\text{H}_2\text{O}$ were separately dissolved in two plastic tubes, respectively, which contained 25 mL of water and 25 mL of ethanol (50 mL in total) [18].

2.4. pH-controlled synthesis

Particles of Ag_2MoO_4 were synthesized by dissolving 2 mmol of AgNO_3 and 1 mmol of H_2MoO_4 . During this procedure, the acid was dissolved in 50 mL of deionized water under stirring. The solution was subsequently added to the AgNO_3 that was dissolved in 50 mL of deionized water [18]. Drops of 3 M KOH were added to this mixture under constant stirring, resulting in a pH of 8.5. The mixture was subsequently transferred to a polytetrafluoroethylene (PTFE) autoclave and held at 150 °C for 1 h. The samples were washed and dried using the same procedure as that described in Section 2.2. A violet precipitate was also observed during this stage. The samples prepared by this procedure were denoted as $\beta\text{-Ag}_2\text{MoO}_4\text{-pH}$.

2.5. Characterizations

The powders obtained were characterized by X-ray diffraction (XRD) using a Rigaku diffractometer (Model D/Max-2500 PC); $\text{Cu K}\alpha$ radiation was used over a 2-theta range of 5–90°, under a rate of 0.02°/min. The size and surface morphology of the particles were analyzed using a field-emission scanning electron microscope (FE-SEM, JEOL JSM 7500F). The morphology and dimensions of the samples were examined using a field-emission-gun scanning electron microscope (FE-SEM, SupraTM 35, Zeiss) operated at 2 kV. The samples were dispersed in acetone, sonicated for 10 min, and finally deposited onto a Si substrate. Using ASAP 2010 equipment (Micromeritics, USA), the Brunauer–Emmett–Teller (BET) surface area was determined at 77 K via nitrogen adsorption–desorption isotherms. Nitrogen, carbon, hydrogen content of materials was estimated by CHN Analyzer using Perkin Elmer 2400 elemental analyzer. Fourier transform (FT)-Raman spectra were obtained at room temperature using a Horiba Jobin-Yvon micro-Raman spectrometer equipped with a microscope; the excitation source was provided by a 514.5 nm wavelength argon laser beam. DRS/UV–Vis spectra were obtained at room temperature in the diffuse reflectance mode using a Varian Cary 5G, and the Kubelka–Munk equation was applied [24]. The band gaps of the solid materials were determined according to the Tauc method [25].

2.6. Photocatalysis assays

To perform the photocatalysis experiments, 50 mL of a RhB solution (10 mg L^{-1}), with a pH of 6.0, was mixed with 50 mg of the photocatalyst. The mixture, consisting of the dye and photocatalyst, was irradiated in a dark box using a UV-lamp located at a distance of 20 cm from the mix. Six parallel mercury-vapor lamps (Philips, 15 W) were used as the UV-C radiation source. Before the UV illumination, the suspensions were stirred in an ultrasound bath (42 kHz, model 1510, Branson, USA) via sonication for 10 min. Every 30 min, a 1 mL aliquot of the suspension was removed from the photocatalytic system and placed in a plastic tube, which was centrifuged at 7000 rpm for 10 min to separate the solid catalyst from the liquid phase. Finally, the

kinetic of the dye photodegradation was monitored in a commercial quartz cuvette via UV–Vis spectroscopy (JASCO V-660) at 554 nm. Subsequently, this procedure was performed for each synthesized β - Ag_2MoO_4 sample.

2.7. Antimicrobial assays

A standard strain of *Escherichia coli* (*E. coli*) (ATCC 8739) was used to evaluate the antibacterial effects of the various samples obtained in this work. Overnight, the *E. coli* cultures were grown in 10 mL of Mueller-Hinton broth (MHB) at 37 °C for 16 h. Following incubation, the *E. coli* bacteria were centrifuged at 4000 rpm for 5 min, washed twice using phosphate-buffered saline (PBS, pH 7.2), and then resuspended in the MHB. The antibacterial properties of the β - Ag_2MoO_4 particles were evaluated by determining the MIC and MBC using a broth microdilution assay, as described by the Clinical and Laboratory Standards Institute (CLSI, document M7-A7, 2006), with some modifications [26,27].

The MIC and MBC values were determined by incubating *E. coli* that were exposed to serial 2-fold dilution in the MHB with the particles (from 1000 $\mu\text{g}/\text{mL}$ to 0.48 $\mu\text{g}/\text{mL}$) in a 96-well microtiter plate at 37 °C for 24 h. The MIC value was determined as the lowest concentration at which there was no visible growth. To determine the MBC value, an aliquot was removed from each well, 10 fold-diluted (10^{-1} to 10^{-8}) and inoculated (25 μL), in duplicate, on Mueller-Hinton agar (MHA). The positive control sample consisted of inoculated MHB without the particles, while uninoculated MHB was used as the negative control sample. Following incubation at 37 °C for 48 h, the colony-forming units per milliliter (CFU/mL) were then calculated and \log_{10} transformed. The presence of β - Ag_2MoO_4 particles was enough to inhibit bacterial growth, and it was not used the UV irradiation lamp.

The MBC value was defined as the lowest concentration of particles at which there was no bacterial growth. To investigate the possible effect of the particles on the biofilm formation, the nanoparticle solution with the lowest MIC and MBC values were evaluated, using FE-SEM, concerning the *E. coli* biofilm formation. To achieve this, *E. coli* cells were spectrophotometrically standardized in MHB at 1×10^7 CFU/mL. Initially, aliquots (1000 μL) of this standardized suspension were placed in the wells of 24-well microtiter plates and maintained at 37 °C for 90 min within an orbital shaker. This step was performed to allow the *E. coli* cells to adhere to the base of the 24-well plate initially; this is known as the adhesion phase. Subsequently, the non-adhered cells were removed by washing with 1000 μL of PBS twice. The experimental wells were then filled with 1000 μL of fresh MHB, containing β - Ag_2MoO_4 -Ethanol solution at a concentration of 1000 $\mu\text{g}/\text{mL}$, while the control wells were filled with 1000 μL of MHB without the cell suspension. Subsequently, the plates were incubated at 37 °C for 24 h using an orbital shaker at 75 rpm. Following the formation of the biofilm, the wells were washed with 1000 μL of PBS to remove the non-adhered cells. They were then fixed with 2.5% glutaraldehyde in PBS for 24 h, dehydrated in increasing concentrations of ethanol (70, 85, and 90%) for 5 min, respectively, and observed using FE-SEM.

3. Results and discussion

3.1. XRD analysis

The XRD patterns indicate the crystalline structure of the β - Ag_2MoO_4 powders obtained by the microwave-assisted solvo-/hydrothermal method. The indexed peaks in Fig. 1 refer to the cubic phase of the β - Ag_2MoO_4 crystals with lattice constants of $a = b = c = 9.6$ Å and a space group of *Fd-3m*, according to Joint Committee on Powder Diffraction Standards (JCPDS) card no. 76-1747. There were no peaks observed that related to a secondary phase, indicating the formation of a pure phase. The sharp and well-defined peaks suggest that the powders had a high degree of crystallization and/or structural ordering at long-range. When the H_2MoO_4 precursor was used under acidic

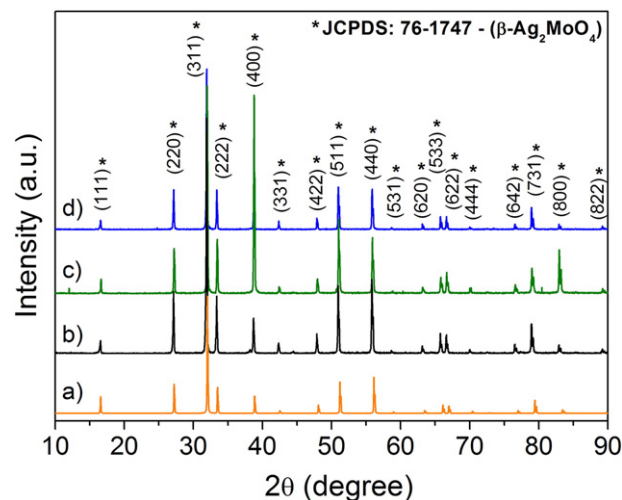


Fig. 1. XRD patterns of the (a) β - Ag_2MoO_4 standard card no. 76-1747, (b) β - Ag_2MoO_4 -pH, (c) β - Ag_2MoO_4 -PVP, and (d) β - Ag_2MoO_4 -Ethanol.

conditions, the formation of the β - Ag_2MoO_4 phase was not observed. However, under basic conditions, the cubic phase was observed (Fig. 1). The appearing of that phase could be because the molybdic acid predominantly exists in an undissociated form under an acidic pH.

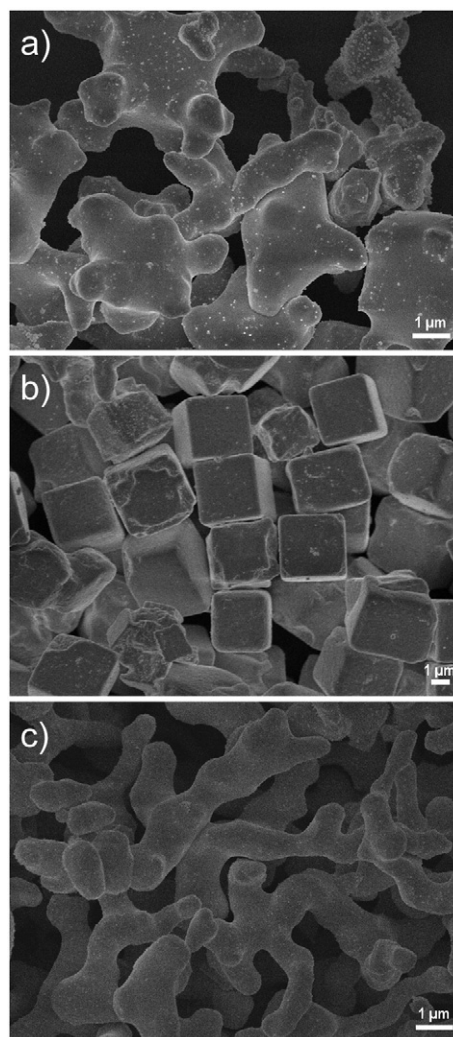


Fig. 2. FE-SEM images of the (a) β - Ag_2MoO_4 -pH, (b) β - Ag_2MoO_4 -PVP and (c) β - Ag_2MoO_4 -Ethanol.

However, the molybdenum oxide dissociates when the pH is increased and becomes solubilized in strong bases, forming the molybdates [28].

3.2. FE-SEM analysis

The β - Ag_2MoO_4 -pH structure (Fig. 2a) present round tips coral-like morphology. Also, the particles are slightly rounded with the greatest width of 4 μm . The final structure form it can be attributed to crystal growth in the aqueous medium and pH adjusted to 8.5. The image of the Fig. 2b shows β - Ag_2MoO_4 -PVP structures with truncated cubic form. Like this, the PVP influenced the final morphology of the geometric structure. The truncated cubes are well-formed and truncated [29], and have edge size of approximately 4 μm . Besides, the truncated cubes microcrystals exhibit homogeneous size. On the other hand, the β - Ag_2MoO_4 -Ethanol structure (Fig. 2c) indicates that the ethanol medium inhibits the particles growth, resulting in their more elongated shape, and each particle has a width and length of approximately 1 μm and 5 μm , respectively. Finally, the structures of Fig. 2a and Fig. 2c show similar morphologies, indicating that the solvent has less influence on the final shape of the particles compared to the effect of PVP polymer as shown in Fig. 2b.

3.3. FT-Raman analysis

Fig. 3 shows the Raman spectra of all β - Ag_2MoO_4 samples. The β - Ag_2MoO_4 -Ethanol and β - Ag_2MoO_4 -PVP materials showed two bands centered at 1340 and 1570 cm^{-1} , which are known as D-band and G-band, respectively, which indicates the presence of carbonaceous residues [30]. The G-band is credited to the stretching mode of carbon sp^2 bonds of well-ordered graphite, while the D-band is attributed to the carbon atoms vibrations with dangling bonds in disordered carbonaceous species [31]. G-band is more intense than D-band, denoting a preponderance of ordered carbon. To confirm this hypothesis, the amount of carbon onto β - Ag_2MoO_4 -pH, β - Ag_2MoO_4 -PVP, and β - Ag_2MoO_4 -Ethanol was determined by CHN elemental analysis (Table 2), resulting in 0.06, 0.23, and 0.91%, respectively. Thus, the detected carbon exists at the material surface as a result of the synthesis process and is not correlated to the β - Ag_2MoO_4 structure.

3.4. DRS/UV-visible spectroscopy

The optical properties of all samples were evaluated using diffuse reflectance UV-vis spectroscopy (DRS/UV-Vis) and are shown in Fig. 4. This analysis provides information about the band gaps and electronic

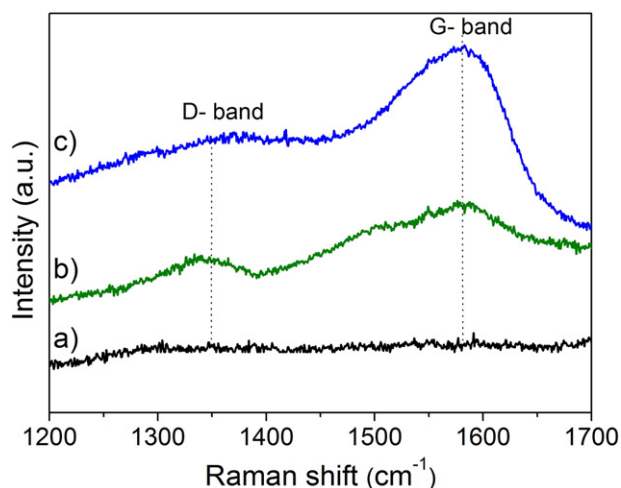


Fig. 3. FT-Raman spectra of the (a) β - Ag_2MoO_4 -pH, (b) β - Ag_2MoO_4 -PVP and (c) β - Ag_2MoO_4 -Ethanol sample in the range of 1200 to 1700 cm^{-1} .

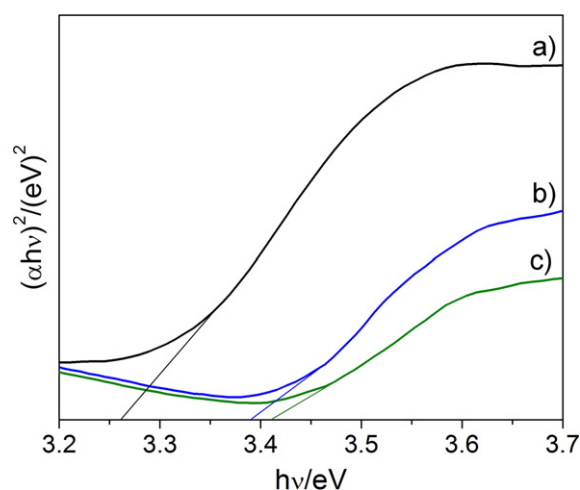


Fig. 4. UV-Vis absorbance spectra of β - Ag_2MoO_4 crystals. (a) β - Ag_2MoO_4 -pH (b) β - Ag_2MoO_4 -Ethanol and (c) β - Ag_2MoO_4 -PVP.

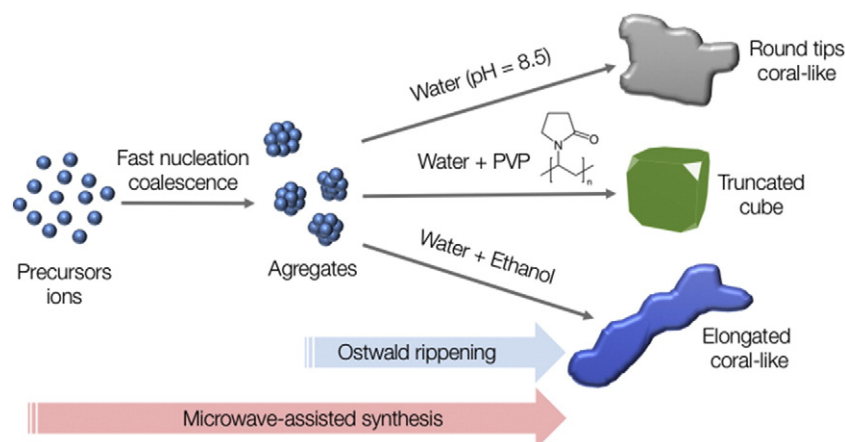
transition states of the semiconductors. The light absorbed by the solid material and the motion of the electrons and holes stimulated by light are crucial features that direct a photocatalytic response, which is relevant to the electronic structure of the active material [32,33]. The optically obtained band gaps were approximately 3.4, 3.2, and 3.4 eV for the β - Ag_2MoO_4 -EtOH, β - Ag_2MoO_4 -pH, and β - Ag_2MoO_4 -PVP, respectively. It was determined that the optical properties of the materials be modified through the use of the various precursors during the synthesis of the Ag_2MoO_4 . The Ag_2MoO_4 -pH exhibited an absorption threshold of 380 nm, which was greater than those of the Ag_2MoO_4 -EtOH and Ag_2MoO_4 -PVP, namely 366 and 364 nm, respectively. The reduction of the absorption band of the samples can be attributed to the presence of carbon owed to the organic precursor on the surface of the particles, as shown in the Raman spectroscopy results (Fig. 3).

3.5. BET analysis

The surface areas of the β - Ag_2MoO_4 -Ethanol, β - Ag_2MoO_4 -pH, and β - Ag_2MoO_4 -PVP samples were determined using the BET method. The largest surface area among the prepared samples was determined for the β - Ag_2MoO_4 -Ethanol, 1.03 m^2/g . The large size of the particles, determined by the FE-SEM analysis, justifies this low value. A smaller crystallite size results in a larger specific surface area [34]. Thus, the large particle sizes of the β - Ag_2MoO_4 -pH and β - Ag_2MoO_4 -PVP samples can be ascribed to their reduced surface areas, 0.63 and 0.09 m^2/g , respectively. The presence of carbon on the surface of the β - Ag_2MoO_4 -PVP sample renders it difficult to perform BET analysis because it significantly reduces the surface area [35]. However, the electron-hole (e^-/h^+) recombination of the samples can be influenced by the various types of defects generated on the surface of the crystals; this probably accelerates the recombination time of the samples [36]. This explains why the β - Ag_2MoO_4 -Ethanol sample has a larger surface area and the inferior photocatalytic result compared with those of the other samples.

3.6. Growth mechanism of structures

Based on the FE-SEM microscopy results, the growth mechanism suggested for the three kinds of structures synthesized by the microwave-assisted solvo-/hydrothermal method is schematized in Scheme 1. The formation of the structures goes through a particular hydro/solvothermal dissolution-recrystallization process, similar to other studies [37–40]. However, during the microwave-assisted crystals growth, the precursor ions coalesce fast and homogeneously [41–43], generating the first nanoparticle aggregates. Furthermore, the high dielectric constant of water favors crystal growth via Ostwald ripening



Scheme 1. An illustration of a growth model for the formation of β - Ag_2MoO_4 structures.

in solution up to its final crystal form. The adjustment of pH to 8.5, induces precipitation of structures with the morphology of the round tips coral-like.

Moreover, the use of the capping polymer as PVP in an aqueous medium culminates in the formation of the β - Ag_2MoO_4 truncated cubes. According to Sun et al. [44], silver nanostructures also grow by Ostwald ripening, and {100} faces are covered with PVP, resulting in anisotropic growth by {111} faces. Therefore, similarly, the crystal habit appearing in β - Ag_2MoO_4 crystals is a result of using the driver polymer which favors the growth of the edges corresponding to the vertex of a truncated

cube, and therefore, the final shape of the crystal is a cube faceted by the plans that grew more slowly.

Finally, also the third morphology shown resembles the form of coral. However, with a smaller width dimension and more elongated compared with the structure obtained in an aqueous medium. In this last morphology, growth process occurred a mixture of water with ethanol. This reaction medium resulted in a decrease in the final particle sizes of β - Ag_2MoO_4 influenced by the lower dielectric constant of ethanol. Also, the particle growth via Ostwald ripening also occurs because water and ethanol are susceptible to microwave radiation and cause

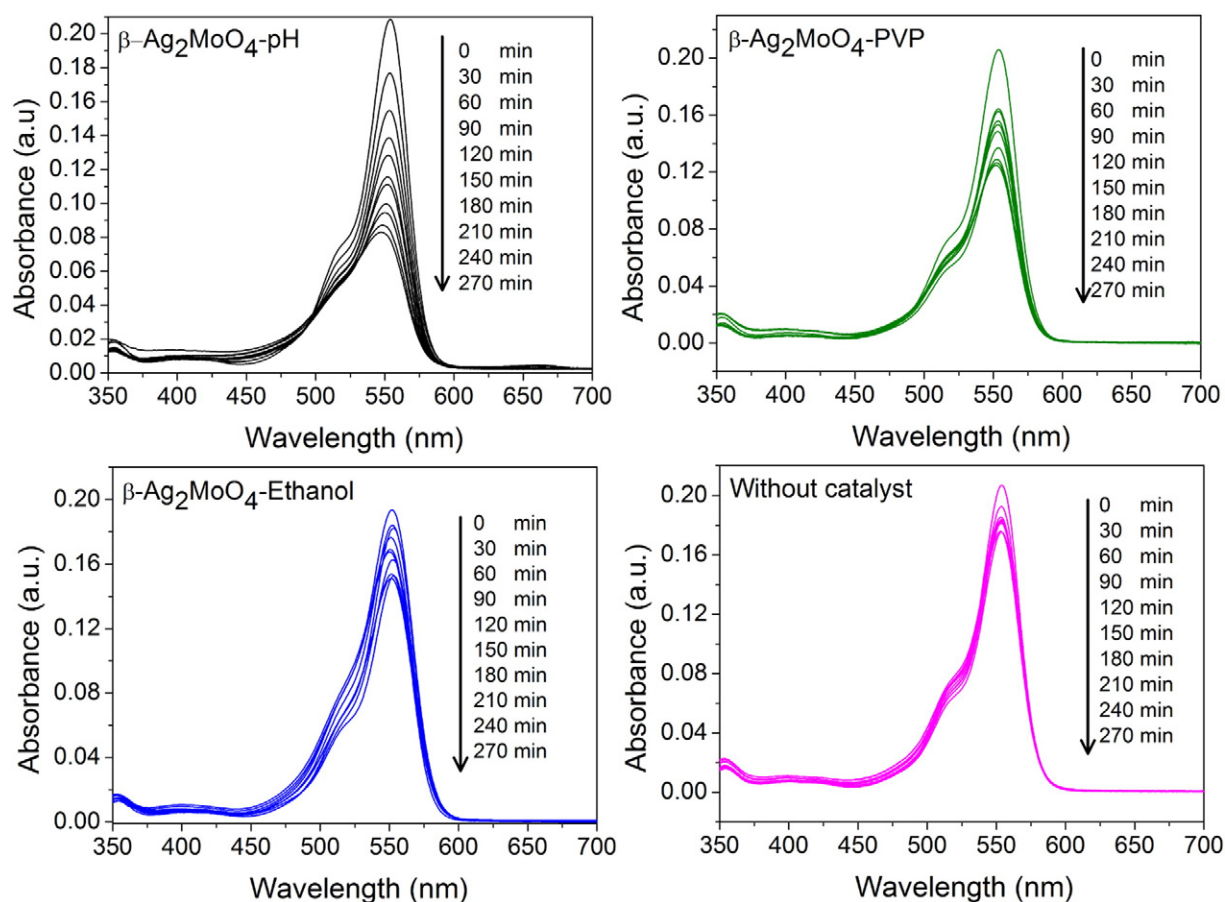


Fig. 5. Absorption spectra of RhB in the presence of β - Ag_2MoO_4 crystals samples.

the rapid and homogeneous heating of the reaction medium, accelerating the dissolution and recrystallization of the precipitates.

3.7. Photocatalytic degradation

The photocatalytic activity of the samples was assessed by the photocatalytic decolorization of the RhB under UV irradiation. The maximum absorption bands of the spectra of the RhB solution were monitored during the photocatalytic reaction process; β - Ag_2MoO_4 -EtOH, β - Ag_2MoO_4 -pH, and β - Ag_2MoO_4 -PVP were used under various irradiation periods. The degradation rates (C_t/C_0) and first-order rate constants (k) of the RhB dye, with and without the catalyst, are also illustrated. Fig. 6a–b shows the photolysis of the RhB under UV irradiation. The control experiment showed that without a photocatalyst, the RhB hardly decomposed during photolysis over a period of 270 min. For the monitoring, the photodegradation mechanism is necessary to measure the dye degradation without the presence of the photocatalyst. In this case, the dye degradation occurs because of absorption of photons by photolysis [45]. Thus, the photolysis is always reported in photocatalysis control experiments under ultraviolet or visible light [46–48].

Fig. 5 indicates that the RhB dye exhibits one band with maximum absorption at 554 nm. However, Fig. 5(b–d) illustrates a significant decrease in the height of the maximum absorption spectra of the RhB during the photodegradation process. The prepared Ag_2MoO_4 -EtOH, Ag_2MoO_4 -pH, and Ag_2MoO_4 -PVP exhibited moderate activity under UV irradiation; the RhB degraded by 24, 58, and 39% at 240 min, respectively. When the active β - Ag_2MoO_4 surface is covered with carbon, the diffusive transport of the RhB molecules can hamper the entry of light and also the diffusion of reactive molecules to the active site of the catalyst [49]. Hence, the presence of residual carbon on the surfaces of the crystal grains affects the photocatalytic activity compared with that of Ag_2MoO_4 -pH.

Fig. 6(a–b) shows linear plots of the standard kinetic data curves obtained for the RhB dye photodegradation that was achieved with the various samples. The discoloration reaction follows first-order kinetics and can be described by the relationship $d[C]/dt = k[C]$, where $[C]$ is

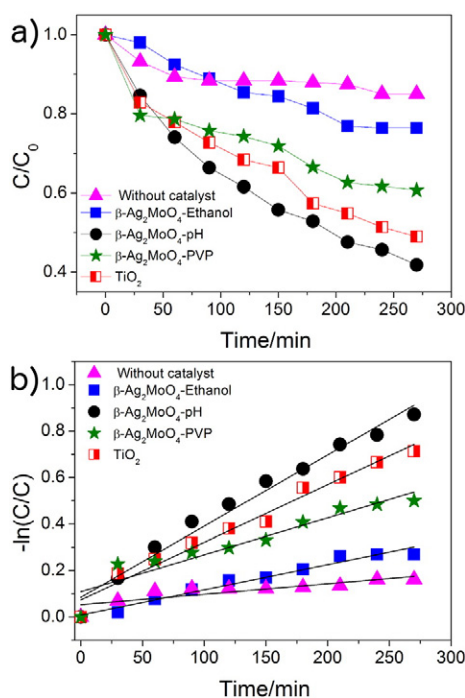


Fig. 6. Photocatalysis degradation profiles of RhB with β - Ag_2MoO_4 crystals (a). First-order kinetics of the samples (b).

Table 1

Rate constant, k , for photocatalysis under UV radiation.

Samples	$k' \times 10^{-3} \text{ (min}^{-1}\text{)}$	R^2
β - Ag_2MoO_4 -pH	3.06	0.9883
β - Ag_2MoO_4 -PVP	1.59	0.9468
β - Ag_2MoO_4 -EtOH	1.08	0.9847
TiO_2 anatase	2.48	0.9716
Without catalyst	0.45	0.8586

the RhB concentration, and k indicates the overall photodegradation rate constant and activity. By plotting $\ln(C/C_0)$ as a function of time through linear regression, where C_0 is the initial concentration of RhB and C is the concentration at time t , we obtained the constant k (min^{-1}) for each sample (Table 1), from the inclines of the simulated straight lines. Table 1 shows the rate constant, k , for the photocatalysis under UV–vis light radiation. However, to obtain a more appropriate comparison to the well-known and widely applied standards, the synthesized materials were compared with commercial TiO_2 anatase (Aldrich, 99.7%) activity, as shown in Fig. 6, and under the same experimental conditions. The commercial TiO_2 in the anatase phase was extensively studied, and it is frequently used as a similar standard for many authors [50–52].

Also, the photocatalytic activity of β - Ag_2MoO_4 is strongly influenced by the presence of carbon, thereby to check the difference the photocatalytic activity between the β - Ag_2MoO_4 -Ethanol and Ag_2MoO_4 -PVP CHN (carbon, hydrogen, nitrogen) analysis (Table 2) was performed to determine the amount of carbon present in each material. Like this, as expected, the β - Ag_2MoO_4 -Ethanol showed a greater amount of carbon in its structure, followed by β - Ag_2MoO_4 -PVP and β - Ag_2MoO_4 -pH.

3.8. Antibacterial study

The antibacterial effect of the β - Ag_2MoO_4 particles on the *E. coli* was evaluated using standard assays, by determining the MIC and MBC. The MIC and MBC values obtained for the particles against a planktonic culture of *E. coli* are presented in Table 3. The results indicate that the three types of β - Ag_2MoO_4 particles were able to inhibit the visual growth of the *E. coli* (MIC values) and kill the bacteria (MBC values). Therefore, the β - Ag_2MoO_4 particles exhibited bacteriostatic and bactericide effects on the *E. coli* cells (Table 3). However, these effects varied depending on the concentrations and types of particles, as demonstrated in Fig. 7a–c.

Additionally, the FE-SEM images demonstrate that the β - Ag_2MoO_4 -Ethanol particles also exhibit an anti-biofilm effect, as shown in Fig. 8. In the image of the control group (Fig. 8a), it is possible to observe a well-formed *E. coli* biofilm, produced by the cohesion of a vast number of cells. Furthermore, the biofilm that was exposed to the β - Ag_2MoO_4 -

Table 2

Elemental analysis of the β - Ag_2MoO_4 -pH β - Ag_2MoO_4 -PVP, and β - Ag_2MoO_4 -Ethanol.

Samples	Carbon (%)	Hydrogen (%)	Nitrogen (%)
β - Ag_2MoO_4 -pH	0.06	0.08	0.05
β - Ag_2MoO_4 -PVP	0.23	0.06	0.09
β - Ag_2MoO_4 -Ethanol	0.91	0.07	0.12

Table 3

MIC and MBC values of particles.

Samples	Antibacterial concentrations	
	MIC ($\mu\text{g/mL}$)	MBC ($\mu\text{g/mL}$)
β - Ag_2MoO_4 -pH	31.25	125
β - Ag_2MoO_4 -PVP	3.9	250
β - Ag_2MoO_4 -EtOH	3.9	31.25

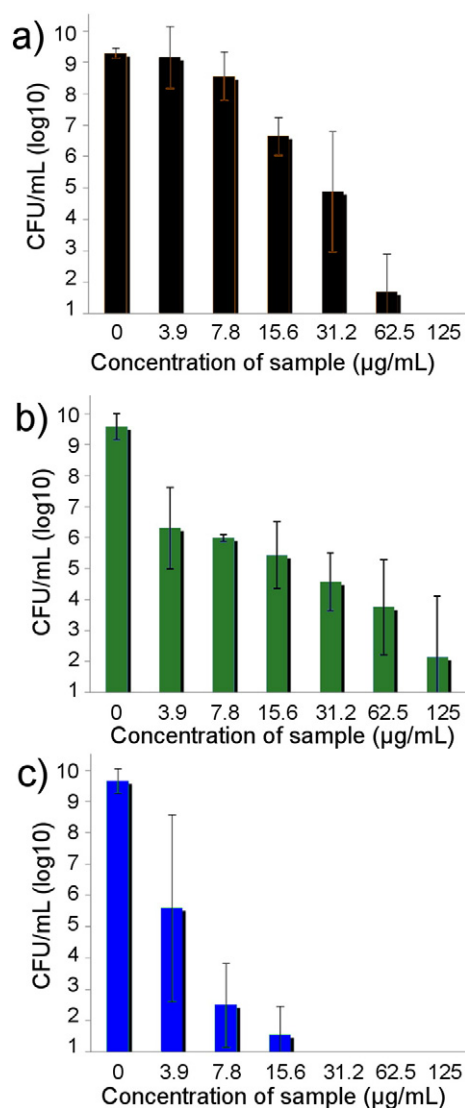


Fig. 7. Mean values of log₁₀ (CFU/mL) of planktonic cultures of *E. coli* exposed to (a) β -Ag₂MoO₄-pH, (b) β -Ag₂MoO₄-PVP, and (c) β -Ag₂MoO₄-Ethanol. Errors bars: standard deviation.

Ethanol particles exhibits an altered architecture with sparse mono-layers of cells (Fig. 8b). Under natural conditions, the microorganisms commonly exist as biofilms that are attached to the surface of microbial communities, which are surrounded by an extracellular polymeric matrix. Under these circumstances, the microorganisms exhibit different characteristics to those of planktonic cells, including increased resistance to host defense mechanisms as well as to antimicrobial agents [53]. Thus, the anti-biofilm properties of the β -Ag₂MoO₄-Ethanol particles observed in this study highlight the potential use of these particles for biomedical applications.

3.9. Photodegradation and antibacterial mechanisms

The photocatalytic and antibacterial performance of the β -Ag₂MoO₄ sample can be attributed to its cluster-like structure and is also supported by the variation in the distributions and densities of extrinsic and intrinsic structural defects within the structures of the surface and bulk materials (Scheme 2). To achieve splitting of the electron-hole pairs in the solid material, the electrons or holes should migrate via cluster-to-cluster charge transfer (CCCT) from the [MoO₄]_o/[MoO₄]_d or [AgO₆]_o/[AgO₆]_d. The complex clusters could be rearranged to increase the photocatalytic or antibacterial efficiency. Therefore, the effect of

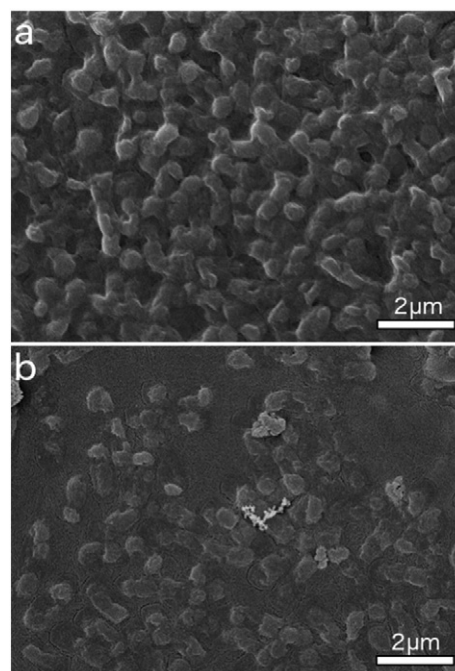
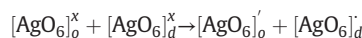
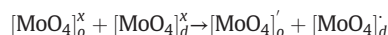


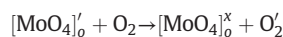
Fig. 8. FE-SEM images of *E. coli* biofilms grown in the presence of the β -Ag₂MoO₄-Ethanol solution: (a) 1000 µg/mL, and (b) 0 µg/mL (control). N: β -Ag₂MoO₄-Ethanol particles.

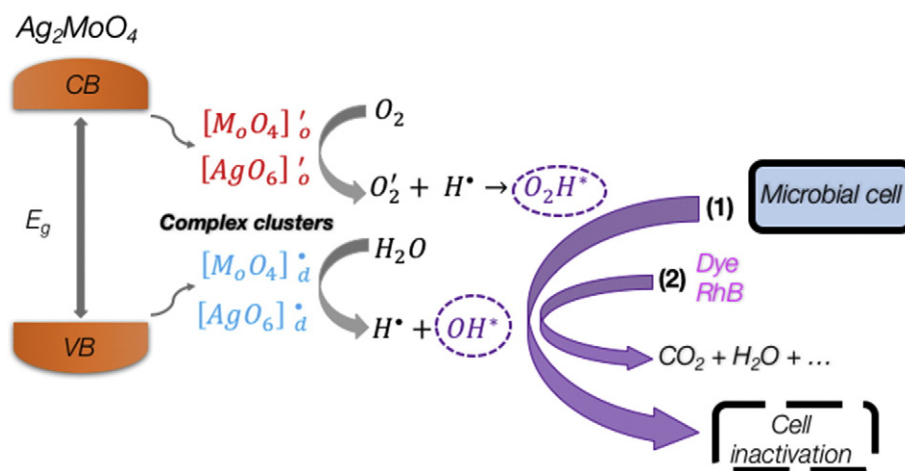
surface defects on the photocatalytic performance and microbial cell inactivation should be considered concerning the [MoO₄]_o, [AgO₆]_o, [MoO₄]_d, and [AgO₆]_d clusters, where o = order and d = disorder. The first effects are inherent to the Ag₂MoO₄ structure and result from the existence of an asymmetric distorted [MoO₄]_d and [AgO₆]_d bulk/surface composition, or ordered [MoO₄]_o and [AgO₆]_o bulk/surface composition. There are interactions between complexes defects of crystals Ag₂MoO₄ and the [AgO₆]_o clusters that may change the effectiveness and mechanism of antibacterial activity. In the study described here, the most important process occurs in the bulk-surface interface and involves the formation of superoxide ion (O₂^{•-}), OOH^{*} radicals and hydrogen ions (H⁺) through of electron-hole transfers process, which causes protein inactivation and consequently cell death [20,22]. In addition, recent studies have demonstrated that Ag-based compounds show broad-spectrum activity and low propensity for inducing microbial resistance [54–56].

The well-ordered complex clusters primarily function as electron drains, easing the charge splits within the semiconductor material. Thus, these polarons can be discharged to acceptors (O₂), and (H₂O), which moderately lowers the reduction potential at the interface. Thereby, the influence of the surface of the material on the photocatalytic and antibacterial activity can be described by the reactions of the clusters:

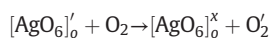


Polaron electron-hole pairs are created at the bulk-surface interface. The charge carriers near the surface, where the charge migrates between the imperfect or ordered surface and the adsorbed molecular O₂, create several types of charged species, including the superoxide ion (O₂^{•-}). The reactions between the [MoO₄]_o or [AgO₆]_o, and the molecular O₂ produce the following types of clusters:

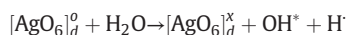
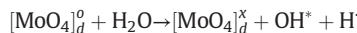




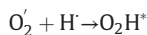
Scheme 2. Proposed RhB photodegradation and microbial cell inactivation mechanisms based on the semiconductor band gap structure and electron–hole pair cluster-to-cluster transference in β - Ag_2MoO_4 .



The water molecules interact with the disordered β - Ag_2MoO_4 clusters and are split into active hydroxyl radicals (OH^*) and ionic hydrogen, corresponding with the reactions:



The initial products of the partial oxidation reaction between the water molecules and complex clusters ($[\text{MoO}_4]_d^o$ or $[\text{AgO}_6]_d^o$) result in the production of hydroxyl radicals (OH^*). These radicals present high oxidation potential and result in the mineralization of dyes or microbial cell inactivation [20,57]. The generated superoxide species (O_2') react with H^+ ions and produce hydrogen peroxide radicals (O_2H^*):



The OH^* and O_2H^* radical species also result in the oxidation of organic compounds, such as dyes, and help to destroy the cells of microorganisms [21,57]. Thus, it is a challenge to correlate the surface/bulk defects with the photocatalytic or antibacterial activity. It is important to ensure that the defects above occur in most disordered/distorted β - Ag_2MoO_4 , with the exclusion of perfect single crystals.

4. Conclusions

Here, an efficient microwave-assisted solvo-/hydrothermal synthetic method was used to design β - Ag_2MoO_4 with controlled morphologies, offering a simple method for the production of various structures, where a more challenging synthesis route was previously required. We have prepared multifunctional β - Ag_2MoO_4 morphologies and demonstrated photocatalytic and antibacterial activity. Among the samples, the β - Ag_2MoO_4 -pH sample exhibited the best photocatalytic results. However, the β - Ag_2MoO_4 -EtOH sample presented superior antibacterial activity. It is important to note that the chemical environment strongly influences the growth and morphology of the crystals. By altering the parameters, such as the surfactants and solvents used, the microcrystals can be synthesized with various forms and/or morphologies by modifying the surface energies of the faces of the crystals. Therefore, to develop functional materials, it is important to control their morphology and structure.

Acknowledgements

The authors acknowledge the São Paulo Research Foundation (FAPESP), grants #2014/17343-0, #2013/07296-2, and #2012/09980-5; and National Council for Scientific and Technological Development (CNPq), grant #444926/2014-3.

References

- [1] J. Tian, P. Hao, N. Wei, H.Z. Cui, H. Liu, 3D Bi_2MoO_6 nanosheet/ TiO_2 nanobelt heterostructure: enhanced photocatalytic activities and photoelectrochemistry performance, *ACS Catal.* 5 (8) (2015) 4530–4536, <http://dx.doi.org/10.1021/acs.catal.5b00560>.
- [2] L. Mohapatra, K. Parida, M. Satpathy, Molybdate/tungstate intercalated oxo-bridged Zn/Y LDH for solar light induced photodegradation of organic pollutants, *J. Phys. Chem. C* 116 (24) (2012) 13063–13070, <http://dx.doi.org/10.1021/jp300066g>.
- [3] R. Adhikari, G. Gyawali, T.H. Kim, T. Sekino, S.W. Lee, Synthesis of Er^{3+} loaded barium molybdate nanoparticles: a new approach for harvesting solar energy, *Mater. Lett.* 91 (2013) 294–297, <http://dx.doi.org/10.1016/j.matlet.2012.10.004>.
- [4] D. Chen, Q. Hao, Z. Wang, H. Ding, Y. Zhu, Influence of phase structure and morphology on the photocatalytic activity of bismuth molybdates, *CrystEngComm* 18 (11) (2016) 1976–1986, <http://dx.doi.org/10.1039/C6CE00264A>.
- [5] C.C. Mardare, D. Tanasic, A. Rathner, N. Müller, A.W. Hassel, Growth inhibition of *Escherichia coli* by zinc molybdate with different crystalline structures, *Phys. Status Solidi* 213 (6) (2016) 1471–1478, <http://dx.doi.org/10.1002/pssa.201532786>.
- [6] H. Tang, A. Lu, L. Li, W. Zhou, Z. Xie, L. Zhang, Highly antibacterial materials constructed from silver molybdate nanoparticles immobilized in chitin matrix, *Chem. Eng. J.* 234 (2013) 124–131, <http://dx.doi.org/10.1016/j.cej.2013.08.096>.
- [7] Y. Meng, Z. Xiong, Preparation of molybdates with antibacterial property, *Key Eng. Mater.* Trans Tech Publications, Aedermannsdorf, Switzerland 2008, pp. 1516–1518.
- [8] M.-C. Liu, L.-B. Kong, C. Lu, X.-M. Li, Y.-C. Luo, L. Kang, Facile fabrication of CoMoO_4 nanorods as electrode material for electrochemical capacitors, *Mater. Lett.* 94 (2013) 197–200, <http://dx.doi.org/10.1016/j.matlet.2012.12.057>.
- [9] L. Cheng, Q. Shao, M. Shao, X. Wei, Z. Wu, Photoswitches of one-dimensional Ag_2MoO_4 ($M = \text{Cr}, \text{Mo}, \text{and W}$), *J. Phys. Chem. C* 113 (5) (2009) 1764–1768, <http://dx.doi.org/10.1021/jp808907e>.
- [10] J. Bi, L. Wu, Y. Zhang, Z. Li, J. Li, X. Fu, Solvothermal preparation, electronic structure and photocatalytic properties of PbMoO_4 and SrMoO_4 , *Appl. Catal. B Environ.* 91 (1–2) (2009) 135–143, <http://dx.doi.org/10.1016/j.apcatb.2009.05.016>.
- [11] G. Gyawali, R. Adhikari, B. Joshi, T.H. Kim, V. Rodríguez-González, S.W. Lee, Sonochemical synthesis of solar-light-driven Ag-PbMoO_4 photocatalyst, *J. Hazard. Mater.* 263 (Pt 1) (2013) 45–51, <http://dx.doi.org/10.1016/j.jhazmat.2013.03.065>.
- [12] J. Zhang, H. Zhang, H. Yang, Z.L. Wang, Sol-gel synthesis and luminescence properties of $\text{ZnMoO}_4:\text{Tb}^{3+}$ nano-structural materials, *Asian J. Chem.* 25 (7) (2013) 4022–4024.
- [13] D.P. Singh, B. Sirota, S. Talpatra, P. Kohli, C. Rebholz, S.M. Aouadi, Broom-like and flower-like heterostructures of silver molybdate through pH controlled self assembly, *J. Nanopart. Res.* 14 (4) (2012) 781, <http://dx.doi.org/10.1007/s11051-012-0781-0>.
- [14] G. Nagaraju, G.T. Chandrappa, J. Livage, Synthesis and characterization of silver molybdate nanowires, nanorods and multipods, *Bull. Mater. Sci.* 31 (3) (2008) 367–371, <http://dx.doi.org/10.1007/s12034-008-0057-6>.
- [15] Z. Li, X. Chen, Z.-L. Xue, Microwave-assisted hydrothermal synthesis of cube-like $\text{Ag-Ag}_2\text{MoO}_4$ with visible-light photocatalytic activity, *Sci. China Chem.* 56 (4) (2013) 443–450, <http://dx.doi.org/10.1007/s11426-013-4845-5>.

- [16] C.H.B. Ng, W.Y. Fan, Uncovering metastable α - Ag_2MoO_4 phase under ambient conditions. Overcoming high pressures by 2,3-bis(2-pyridyl)pyrazine doping, *Cryst. Growth Des.* 15 (6) (2015) 3032–3037, <http://dx.doi.org/10.1021/acs.cgd.5b00455>.
- [17] M.T. Fabbro, C.C. Foggi, L.P.S. Santos, L. Gracia, A. Perrin, C.E. Vergani, A.L. Machado, J. Andres, E. Cordocillo, E. Longo, Synthesis, antifungal evaluation and optical properties of silver molybdate microcrystals in different solvents: a combined experimental and theoretical study, *Dalton Trans.* 45 (26) (2016) 10736–10743, <http://dx.doi.org/10.1039/C6DT00343E>.
- [18] A.F. Gouveia, J.C. Sczancoski, M.M. Ferrer, A.S. Lima, M.R.M.C. Santos, M.S. Li, R.S. Santos, E. Longo, L.S. Cavalcante, Experimental and theoretical investigations of electronic structure and photoluminescence properties of β - Ag_2MoO_4 microcrystals, *Inorg. Chem.* 53 (11) (2014) 5589–5599, <http://dx.doi.org/10.1021/ic500335x>.
- [19] D. Wang, L. Guo, Y. Zhen, L. Yue, G. Xue, F. Fu, AgBr quantum dots decorated mesoporous Bi_2WO_6 architectures with enhanced photocatalytic activities for methylene blue, *J. Mater. Chem. A* 2 (30) (2014) 11716, <http://dx.doi.org/10.1039/C4TA01444H>.
- [20] R.S. André, C.A. Zamperini, E.G. Mima, V.M. Longo, A.R. Albuquerque, J.R. Sambrano, A.L. Machado, C.E. Vergani, A.C. Hernandez, J.A. Varela, E. Longo, Antimicrobial activity of TiO_2 :Ag nanocrystalline heterostructures: experimental and theoretical insights, *Chem. Phys.* 459 (2015) 87–95, <http://dx.doi.org/10.1016/j.chemphys.2015.07.020>.
- [21] Y.N. Chang, J.L. Gong, G.M. Zeng, X.M. Ou, B. Song, M. Guo, J. Zhang, H.Y. Liu, Antimicrobial behavior comparison and antimicrobial mechanism of silver coated carbon nanocomposites, *Process. Saf. Environ. Prot.* 102 (2016) 596–605, <http://dx.doi.org/10.1016/j.psep.2016.05.023>.
- [22] W.K. Jung, H.C. Koo, K.W. Kim, S. Shin, S.H. Kim, Y.H. Park, Antibacterial activity and mechanism of action of the silver ion in *Staphylococcus aureus* and *Escherichia coli*, *Appl. Environ. Microbiol.* 74 (7) (2008) 2171–2178, <http://dx.doi.org/10.1128/AEM.02001-07>.
- [23] Longo da Silva, E.; Arana Varela, J.; de Araujo Almeida, D. K.; Paschoalini Volanti, D. Microwave aided device for hydrothermal synthesis of nanostructured oxides, particularly obtaining particles of metal oxides, comprises container, in which hydrothermal reaction takes place, and lid for container. BR200815393-A2, 07 Dec 2010.
- [24] V. Džimbeg-malčić, Ž. Barbarić-mikočević, K. Itrić, Kubelka-Munk theory in describing optical properties of paper (1), *Tech. Gaz.* 18 (1) (2011) 117–124.
- [25] D.L. Wood, J. Tauc, Weak absorption tails in amorphous semiconductors, *Phys. Rev. B* 5 (8) (1972) 3144.
- [26] NCCLS, Performance Standards for Antimicrobial Susceptibility Testing, 2007 (doi:1-56238-525-5).
- [27] C. Clinical and Laboratory Standards Institute, Reference method for broth dilution antifungal susceptibility testing of yeasts; third informational supplement - M27-S3, *Clin. Lab. Standards Inst. - NCCLS* 28 (2008).
- [28] C. Sjöstedt, T. Wällstedt, J.P. Gustafsson, H. Borg, Speciation of aluminium, arsenic and molybdenum in excessively limed lakes, *Sci. Total Environ.* 407 (18) (2009) 5119–5127, <http://dx.doi.org/10.1016/j.scitotenv.2009.05.034>.
- [29] Y. Xia, Y. Xiong, S.E. Skrabalak, Shape-controlled synthesis of metal nanocrystals: simple chemistry meets complex physics? *Angew. Chem. Int. Ed.* 48 (1) (2009) 60–103, <http://dx.doi.org/10.1002/anie.200802248>.
- [30] L. Zhang, R.V. Koka, A study on the oxidation and carbon diffusion of TiC in alumina-titanium carbide ceramics using XPS and Raman spectroscopy, *Mater. Chem. Phys.* 57 (1) (1998) 23–32, [http://dx.doi.org/10.1016/S0254-0584\(98\)00187-4](http://dx.doi.org/10.1016/S0254-0584(98)00187-4).
- [31] A.E. Galetti, M.F. Gomez, L.A. Arrúa, M.C. Abello, Hydrogen production by ethanol reforming over NiZnAl catalysts. Influence of Ce addition on carbon deposition, *Appl. Catal. A Gen.* 348 (1) (2008) 94–102, <http://dx.doi.org/10.1016/j.apcata.2008.06.039>.
- [32] G. Botelho, J.C. Sczancoski, J. Andres, L. Gracias, E. Longo, Experimental and theoretical study on the structure, optical properties, and growth of metallic silver nanostructures in Ag_3PO_4 , *J. Phys. Chem. C* 119 (11) (2015) 6293–6306, <http://dx.doi.org/10.1021/jp512111v>.
- [33] T. Zhu, S.-P. Gao, The stability, electronic structure, and optical property of TiO_2 polymorphs, *J. Phys. Chem. C* 118 (21) (2014) 11385–11396, <http://dx.doi.org/10.1021/jp412462m>.
- [34] C. Wang, Z. Huang, Controlled synthesis of α - Fe_2O_3 nanostructures for efficient photocatalysis, 164 (2016) 194–197, <http://dx.doi.org/10.1016/j.matlet.2015.10.152>.
- [35] S. Caramunt, A. Varela, D. López-Díaz, M.M. Velázquez, A. Cornet, A. Cirera, The importance of interbands on the interpretation of the Raman spectrum of graphene oxide, *J. Phys. Chem. C* 119 (18) (2015) 10123–10129, <http://dx.doi.org/10.1021/acs.jpcc.5b01590>.
- [36] B. Ohtani, Y. Ogawa, S. Nishimoto, Photocatalytic activity of amorphous - anatase mixture of titanium (IV) oxide particles suspended in aqueous solutions, *J. Phys. Chem. B* 111 (19) (1997) 3746–3752, <http://dx.doi.org/10.1021/jp962702+>.
- [37] M. Lin, Z.Y. Fu, J.P.Y. Tan, H.R. Tan, S.C. Ng, E. Teo, J.P.Y. Tan, S.C. Ng, E. Teo, Hydrothermal synthesis of CeO_2 nanocrystals: ostwald ripening or oriented attachment? *Cryst. Growth Des.* 12 (6) (2012) 3296–3303, <http://dx.doi.org/10.1021/cg300421x>.
- [38] J.J. Qi, S. Gao, K. Chen, J. Yang, H.W. Zhao, L. Guo, S.H. Yang, Vertically aligned, double-sided, and self-supported 3D WO_3 nanocolumn bundles for low-temperature gas sensing, *J. Mater. Chem. A* 3 (35) (2015) 18019–18026, <http://dx.doi.org/10.1039/C5TA03711E>.
- [39] G.J. Wilson, A.S. Matijasevich, D.R.G. Mitchell, J.C. Schulz, G.D. Will, Modification of TiO_2 for enhanced surface properties: finite ostwald ripening by a microwave hydrothermal process, *Langmuir* 22 (5) (2006) 2016–2027.
- [40] W. Wu, S. Zhang, J. Zhou, X. Xiao, F. Ren, C. Jiang, Controlled synthesis of monodisperse sub-100 nm hollow SnO_2 nanospheres: a template- and surfactant-free solution-phase route, the growth mechanism, optical properties, and application as a photocatalyst, *Chem. - A Eur. J.* 17 (35) (2011) 9708–9719, <http://dx.doi.org/10.1002/chem.201100694>.
- [41] A.P. de Moura, R.C. Lima, M.L. Moreira, D.P. Volanti, J.W.M. Espinosa, M.O. Orlandi, P.S. Pizani, J.A. Varela, E. Longo, ZnO architectures synthesized by a microwave-assisted hydrothermal method and their photoluminescence properties, *Solid State Ionics* 181 (15–16) (2010) 775–780, <http://dx.doi.org/10.1016/j.ssi.2010.03.013>.
- [42] D.P. Volanti, M.O. Orlandi, J. Andres, E. Longo, Efficient microwave-assisted hydrothermal synthesis of CuO sea urchin-like architectures via a mesoscale self-assembly, *CrystEngComm* 12 (6) (2010) 1696–1699, <http://dx.doi.org/10.1039/b922978g>.
- [43] X. Zou, H. Fan, Y. Tian, M. Zhang, X. Yan, Microwave-assisted hydrothermal synthesis of $\text{Cu/Cu}_2\text{O}$ hollow spheres with enhanced photocatalytic and gas sensing activities at room temperature, *Dalton Trans.* 44 (17) (2015) 7811–7821, <http://dx.doi.org/10.1039/c4dt03417a>.
- [44] Y. Sun, B. Mayers, T. Herricks, Y. Xia, Polyol synthesis of uniform silver nanowires: a plausible growth mechanism and the supporting evidence, *Nano Lett.* 3 (7) (2003) 955–960, <http://dx.doi.org/10.1021/nl034312m>.
- [45] Z.L. Ye, C.Q. Cao, J.C. He, R.X. Zhang, H.Q. Hou, Photolysis of organic pollutants in wastewater with 206 nm UV irradiation, *Chin. Chem. Lett.* 20 (6) (2009) 706–710, <http://dx.doi.org/10.1016/j.ccl.2008.12.033>.
- [46] J. Zhang, H. Cui, B. Wang, C. Li, J. Zhai, Q. Li, Preparation and characterization of fly ash cenospheres supported CuO-BiVO_4 heterojunction composite, *Appl. Surf. Sci.* 300 (2014) 51–57, <http://dx.doi.org/10.1016/j.apsusc.2014.02.001>.
- [47] P. Madhusudan, J. Ran, J. Zhang, J. Yu, G. Liu, Novel urea assisted hydrothermal synthesis of hierarchical $\text{BiVO}_4/\text{Bi}_2\text{O}_3$ nanocomposites with enhanced visible-light photocatalytic activity, *Appl. Catal. B Environ.* 110 (2011) 286–295, <http://dx.doi.org/10.1016/j.apcatb.2011.09.014>.
- [48] K.-J. Hwang, J.-W. Lee, W.-G. Shim, H.D. Jang, S.-I. Lee, S.-J. Yoo, Adsorption and photocatalysis of nanocrystalline TiO_2 particles prepared by sol-gel method for methylene blue degradation, *Adv. Powder Technol.* 23 (3) (2012) 414–418, <http://dx.doi.org/10.1016/j.apt.2011.05.010>.
- [49] M. Inagaki, F. Kojin, B. Tryba, M. Toyoda, Carbon-coated anatase: the role of the carbon layer for photocatalytic performance, *Carbon N. Y.* 43 (8) (2005) 1652–1659, <http://dx.doi.org/10.1016/j.carbon.2005.01.043>.
- [50] D. Yang, H. Liu, Z. Zheng, Y. Yuan, J. Zhao, E.R. Wacławik, X. Ke, H. Zhu, An efficient photocatalyst structure: $\text{TiO}_2(\text{B})$ nanofibers with a shell of anatase nanocrystals, *J. Am. Chem. Soc.* 131 (49) (2009) 17885–17893, <http://dx.doi.org/10.1021/ja906774k>.
- [51] U.G. Akpan, B.H. Hameed, Parameters affecting the photocatalytic degradation of dyes using TiO_2 -based photocatalysts: a review, *J. Hazard. Mater.* 170 (2–3) (2009) 520–529, <http://dx.doi.org/10.1016/j.jhazmat.2009.05.039>.
- [52] G. Plantard, T. Janin, V. Goetz, S. Brosillon, Solar photocatalysis treatment of phytosanitary refuses: efficiency of industrial photocatalysts, *Appl. Catal. B Environ.* 115–116 (2012) 38–44, <http://dx.doi.org/10.1016/j.apcatb.2011.11.034>.
- [53] G. Sharma, S. Sharma, P. Sharma, D. Chandola, S. Dang, S. Gupta, R. Gabrani, *Escherichia coli* biofilm: development and therapeutic strategies, *J. Appl. Microbiol.* 121 (2) (2016) 309–319, <http://dx.doi.org/10.1111/jam.13078>.
- [54] B. Gao, J. Fu, K. Huo, W. Zhang, Y. Xie, P.K. Chu, Quasi-aligned $\text{Ag-Nb}_2\text{O}_5$ nanobelt arrays with enhanced photocatalytic and antibacterial activities, *J. Am. Ceram. Soc.* 94 (8) (2011) 2330–2338, <http://dx.doi.org/10.1111/j.1551-2916.2010.04370.x>.
- [55] H. Cheng, Y. Li, K. Huo, B. Gao, W. Xiong, Long-lasting in vivo and in vitro antibacterial ability of nanostructured titania coating incorporated with silver nanoparticles, *J. Biomed. Mater. Res. Part A* 102 (10) (2014) 3488–3499, <http://dx.doi.org/10.1002/jbm.a.35019>.
- [56] H. Cheng, W. Xiong, Z. Fang, H. Guan, W. Wu, Y. Li, Y. Zhang, M.M. Alvarez, B. Gao, K. Huo, J. Xu, N. Xu, C. Zhang, J. Fu, A. Khademhosseini, F. Li, Strontium (Sr) and silver (Ag) loaded nanotubular structures with combined osteoinductive and antimicrobial activities, *Acta Biomater.* 31 (2016) 388–400, <http://dx.doi.org/10.1016/j.actbio.2015.11.046>.
- [57] M.R.D. Bomio, R.L. Tranquilin, F.V. Motta, C.A. Paskocimas, R.M. Nascimento, L. Gracia, J. Andres, E. Longo, Toward understanding the photocatalytic activity of PbMoO_4 powders with predominant (111), (100), (011), and (110) facets. A combined experimental and theoretical study, *J. Phys. Chem. C* 117 (41) (2013) 21382–21395, <http://dx.doi.org/10.1021/jp407416h>.